Editors' Suggestion

Broadband electron paramagnetic resonance spectroscopy of ^{167}Er:^{7}LiYF$_4$ at millikelvin temperatures

Ana Strinić,[1,2,3,*] Patricia Oehrl,[1,2,3] Achim Marx,[1] Pavel A. Bushev,[4] Hans Huebl,[1,2,3] Rudolf Gross,[1,2,3] and Nadezhda Kukharchyk[1,2,3,†]

[1]*Walther-Meißner-Institut, Bayerische Akademie der Wissenschaften, 85748 Garching, Germany*
[2]*School of Natural Sciences, Technical University of Munich, 85748 Garching, Germany*
[3]*Munich Center for Quantum Science and Technology (MCQST), 80799 Munich, Germany*
[4]*Institute of Functional Quantum Systems (PGI-13), Forschungszentrum Jülich, 52425 Jülich, Germany*

(Received 17 January 2025; revised 16 April 2025; accepted 2 June 2025; published 20 June 2025)

Rare-earth spin ensembles are a promising platform for microwave quantum memory applications due to their hyperfine transitions, which can exhibit exceptionally long coherence times when using an operation point with zero first-order Zeeman (ZEFOZ) shift. In this work, we use broadband electron paramagnetic resonance (EPR) spectroscopy on ^{167}Er:^{7}LiYF$_4$ single crystals at subkelvin temperatures. By fitting the spin Hamiltonian to the zero-field spectrum, we obtain refined parameters of the magnetic field-independent interactions, such as the hyperfine and quadrupole interaction. We also study the influence of the quadrupole interaction on the hyperfine splitting in the zero and low magnetic field range by analyzing EPR spectra between 0 mT and 50 mT. Our findings highlight the broadband EPR spectroscopy approach as a powerful tool for the precise determination of the spin Hamiltonian parameters and for the characterization of hyperfine transitions in terms of their selection rules and linewidth.

DOI: 10.1103/5j7f-wfyl

I. INTRODUCTION

Hybrid quantum systems consisting of a quantum processor coupled to a quantum memory possess great potential for quantum computing [1,2]. To this end, efficient interfacing of the quantum processor to the quantum memory is essential, implying direct compatibility of their operation conditions and enabling a direct low-loss coupling between both devices. Superconducting quantum processors are operated at GHz frequencies, millikelvin temperatures, and a low magnetic field environment [3,4]. These operation conditions are compatible with several spin-ensemble platforms, such as nitrogen-vacancy color centers in diamond [5,6], donors in silicon [7–9], and rare-earth doped crystals [10–12]. Therefore, these systems are promising candidates for establishing microwave quantum memory devices.

Rare-earth spin ensembles are particularly promising for interfacing microwave quantum memories with superconducting quantum processors based on qubits operating at microwave frequencies. First, they are frequency-matched owing to their zero-field hyperfine transitions in the GHz-frequency range, and second, they can exhibit exceptionally long spin coherence times up to a few milliseconds [13]. These long coherence times are possible by making use of dynamical decoupling pulse sequences [14], probing ultrapure crystals [13], or utilizing transitions with so-called zero first-order Zeeman (ZEFOZ) shift. In the literature, the latter are also referred to as "clock transitions" [15,16]. As ZEFOZ transitions are, to first order, insensitive to magnetic field fluctuations, significantly increased coherence times can be achieved due to the reduced impact of magnetic field noise [17]. They are inherent to many hyperfine transitions of rare-earth ions embedded in various host materials and can be found even at zero and low magnetic field strength [16,18]. However, finding true ZEFOZ transitions can be experimentally challenging due to the complex hyperfine level structure of rare-earth ions [19]. In the same way, the exact theoretical modeling of the hyperfine level structure, allowing to identify transitions suitable for microwave quantum memory applications, requires the precise experimental determination of the parameters as well as the identification of all terms entering the spin Hamiltonian.

Electron paramagnetic resonance (EPR) spectroscopy is a powerful experimental approach to characterize the magnetic properties of electronic spins in solids with high precision. Typically, EPR studies are performed by coupling the spin system to a microwave cavity or resonator and measuring the absorption of a microwave signal while sweeping the externally applied magnetic field. At resonance, the coupling of the spin systems to the resonant mode of the cavity can be detected as a change in the real and imaginary parts of the microwave signal. However, this field-swept approach is limited to a narrow frequency range determined by the narrow

*Contact author: Ana.Strinic@wmi.badw.de
†Contact author: Nadezhda.Kukharchyk@wmi.badw.de

Published by the American Physical Society under the terms of the Creative Commons Attribution 4.0 International license. Further distribution of this work must maintain attribution to the author(s) and the published article's title, journal citation, and DOI.

bandwidth of the microwave resonator. Therefore, in recent years, different broadband techniques have been developed, allowing for sweeping both the magnetic field and microwave frequency and thereby accessing a broad parameter regime. A particularly powerful technique is broadband EPR spectroscopy based on a coplanar transmission line [20–24]. Here, the spin system is placed on top of the transmission line, and the microwave transmission and/or reflection is measured as a function of the applied magnetic field and microwave frequency over a wide range using a vector network analyzer. Such a technique is common for broadband ferromagnetic resonance experiments [25,26].

In this work, we perform broadband EPR spectroscopy on a diluted ^{167}Er:^{7}LiYF$_4$ crystal at millikelvin temperatures to identify the hyperfine transitions of ^{167}Er. We precisely determine the hyperfine and quadrupole parameters of the spin Hamiltonian using a least-squares fit of the measured zero-field spectrum. Moreover, based on the broadband spectra recorded in the magnetic field range 0–50 mT, with the magnetic field $\boldsymbol{B_0}$ aligned along different crystallographic directions of the LiYF$_4$ host crystal, we can confirm the already published g factors. By taking spectra in Faraday- and Voigt-like geometries, we can also probe different selection rules, which we can reliably simulate. We further determine the effective temperature of the spin ensemble. Finally, the broadband spectra allow us to extract the linewidth of the hyperfine transitions. We used these data to get insight into the linewidth narrowing of the hyperfine transitions around their ZEFOZ points.

II. EXPERIMENTAL TECHNIQUES

The experimental setup used for the broadband EPR spectroscopy is schematically shown in Fig. 1(a). We study a ^{167}Er:^{7}LiYF$_4$ crystal with an ^{167}Er concentration of 0.0025%, which was grown using the Bridgman-Stockbarger technique (see Ref. [27]).

The crystal is placed on top of a meander-shaped superconducting coplanar waveguide (CPW). The superconducting circuit is fabricated using niobium sputter deposition on a high-resistivity silicon substrate and subsequent patterning by electron beam lithography and reactive ion etching. The geometry of the CPW with a center conductor width of 20 µm and a gap width of 12 µm also allows us to simulate the distribution of the microwave B_1 excitation field in the proximity of the CPW [see zoom-in in Fig. 1(a)]. The spatial dependence of the normalized magnitude $|B_1|$ highlights the rapid decay of the signal strength with increasing distance from the CPW surface. Therefore, we choose a meander-shaped design to effectively couple the spins to the propagating microwave field and probe a large crystal volume. The CPW is wire-bonded via taper patches to a gold-plated printed circuit board, interfaced to microwave coaxial cables with solderless, nonmagnetic SMA connectors. Throughout the microwave assembly, we aim for an impedance matching of 50 Ω.

The sample assembly is thermally anchored to the mixing-chamber stage of a dry dilution refrigerator (Bluefors, XLD 1000) with a base temperature of less than 10 mK. It is positioned within the bore of a home-built superconducting (NbTi) solenoid magnet [28], which is thermally anchored to the

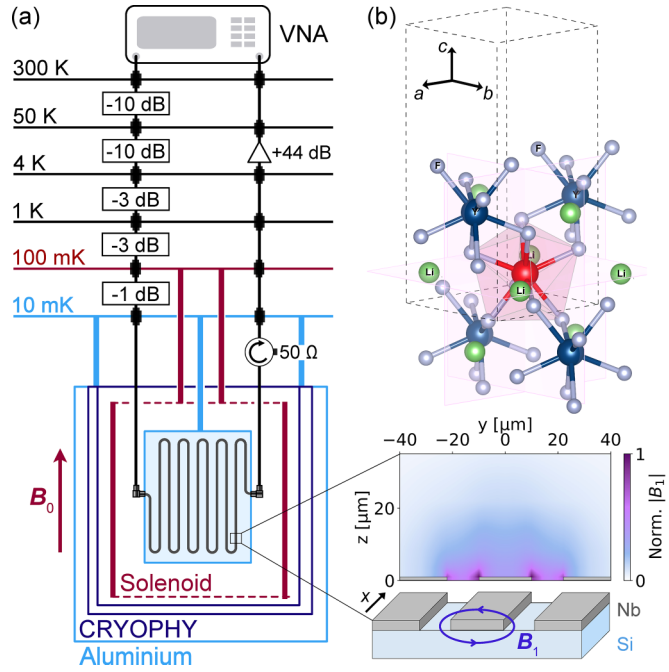


FIG. 1. (a) Schematics of the measurement setup indicating the thermal stages of the dilution refrigerator and the microwave wiring. The studied crystal is placed on top of a meander-shaped CPW in the bore of a superconducting coil producing a magnetic field B_0. A VNA is used to measure the complex transmission parameter S_{21}. Zoom-in: Simulated distribution of the propagating magnetic mode B_1 around the center conductor of the CPW with a current flow in x direction, normalized to its maximum value. (b) Coordination of an Er^{3+}-ion (red) within the unit cell of ^{7}LiYF$_4$ based on published lattice parameters [30,31].

100 mK stage of the dilution refrigerator and can generate a static magnetic field (B_0) up to ±50 mT. In addition, the magnet is enclosed by three layers of magnetic shielding. On the one hand, the magnetic shielding confines the magnetic field within the coil, allowing for compatibility with superconducting qubits operated within the same cryostat. On the other hand, the magnitude of the background magnetic fields at the sample position is strongly reduced, which is crucial for ultralow field EPR spectroscopy.

To probe the selection rules, the spectroscopy measurements have been performed for $\boldsymbol{B_0}$ aligned both parallel and perpendicular to the microwave propagation vector $\boldsymbol{k}$. In the following, we adopt the common nomenclature used for propagating wave experiments and refer to the probed excitation geometries as Faraday-like geometry ($\boldsymbol{k} \parallel \boldsymbol{B_0}$) and Voigt-like geometry ($\boldsymbol{k} \perp \boldsymbol{B_0}$) [29]. Further details of the positioning of the sample on top of the CPW and its alignment are discussed in Appendix C.

The complex microwave transmission S_{21} is measured with a vector network analyzer (VNA). To thermalize the microwave signal with input power $P_{\text{in}} = -50$ dBm to mK temperatures, we attenuate the input line in the dilution refrigerator using a set of attenuators [see Fig. 1(a)] with a total attenuation of 27 dB. The output line is configured with a microwave circulator to reduce the impact of thermal microwave photons from stages with higher temperatures. We

use a low-noise HEMT amplifier at the 4 K stage for the pre-amplification of the output signal. To analyze the magnetic field dependence, we calibrate the applied magnetic field strength via the EPR transition of a 2,2-diphenyl-1-picrylhydrazyl (DPPH) sample (Sigma Aldrich) as described in Appendix B.

III. THEORETICAL BACKGROUND

The host crystal $^7LiYF_4$ belongs to the group of Scheelite crystals with a tetragonal unit cell [32]. When doped with Er^{3+}-ions, these substitute the Y^{3+}-ions while preserving the local S_4 symmetry [31,33]. The coordination of the Er^{3+}-ion within the $^7LiYF_4$ unit cell is indicated in Fig. 1(b). The doping induces low strain due to the similar ionic radii of Er^{3+} and Y^{3+} [34] and does not lead to any charge compensation as both ions are in the trivalent charge state [33]. Exceptionally narrow inhomogeneous broadening has been observed on optical transitions of Er:$^7LiYF_4$. This was attributed to the fact that the influence of crystal defects and strain in isotopically purified $^7LiYF_4$ is so small that the inhomogeneous broadening becomes dominated by the magnetic field fluctuations produced by nuclear spins of fluorine ions [27,35].

The Er^{3+} ([Xe]$4f^{11}$) belongs to the group of Kramers ions. At cryogenic temperatures, only the lowest Kramers doublet ($J = \frac{15}{2}$) of the ground state (spectroscopic notation: $^4I_{15/2}$) is populated, and the spin system can be approximated with an effective spin $S = 1/2$ [36]. In this case, the energy level splitting of the $^{167}Er^{3+}$ ($I = 7/2$) ground state can be described by a spin Hamiltonian containing three main terms: the electron Zeeman interaction (H_{EZ}), the hyperfine interaction (H_{HF}) and, due to the nuclear spin $I > 1/2$, the nuclear quadrupole interaction (H_Q). The corresponding characteristic interaction tensors $\boldsymbol{g}$ and $\boldsymbol{A}$ are compatible with the tetragonal crystal symmetry and, therefore, their components can be expressed as parallel, $g_\parallel$ and $A_\parallel$, and perpendicular, $g_\perp$ and $A_\perp$, to the crystallographic c-axis, when presented in diagonal form [36]. Assuming axial symmetry, the quadrupole interaction tensor $\boldsymbol{Q}$ is traceless and can be described by a single parameter P, which relates to the largest principal value of the electric field gradient at the nucleus [37]. The spin Hamiltonian can be expressed as follows:

$$H_{\text{eff}} = H_{\text{EZ}} + H_{\text{HF}} + H_{\text{Q}} = \mu_{\text{B}} g_\perp (B_x \boldsymbol{S_x} + B_y \boldsymbol{S_y}) + \mu_{\text{B}} g_\parallel B_z \boldsymbol{S_z} + A_\perp (\boldsymbol{S_x I_x} + \boldsymbol{S_y I_y}) + A_\parallel \boldsymbol{S_z I_z} + P\left(\boldsymbol{I_z}^2 - \tfrac{1}{3}\boldsymbol{I}^2\right), \quad (1)$$

with the Bohr magneton μ_B, the applied magnetic field $\boldsymbol{B} = (B_x, B_y, B_z)$, and the electron $(\boldsymbol{S_x}, \boldsymbol{S_y}, \boldsymbol{S_z})$ and nuclear $(\boldsymbol{I_x}, \boldsymbol{I_y}, \boldsymbol{I_z})$ spin operators. By diagonalizing the spin Hamiltonian in Eq. (1) numerically, the eigenenergies and eigenstates, as well as the related hyperfine transitions between these states, are obtained. The transition probability between two states $|i\rangle$ and $|f\rangle$ under the action of a microwave magnetic field $\boldsymbol{B_1}$ is determined by the matrix element of the interaction energy $H_1 = -\mu_B \boldsymbol{B_1} \boldsymbol{g} \hat{\boldsymbol{S}}$ [38]. The intensity I_{if} of the corresponding spectroscopic line observed in an EPR experiment is proportional to

$$I_{if} \propto \chi \, |\langle f|H_1|i\rangle|^2. \quad (2)$$

TABLE I. Summary of the published spin Hamiltonian parameters for Er:$LiYF_4$ as well as those determined in this work.

Source	$g_\parallel$	$g_\perp$	$A_\parallel$ (MHz)	$A_\perp$ (MHz)	P (MHz)
[39]	3.32	8.09			
[32]	3.137	8.105	325.8	840	
[35]	3.132	8.102			
[40]	3.130	7.929	325	816	
[46]	3.141	7.932	334[a]	824[a]	
[41]	3.147	8.105			
[43]	3.132	8.102			
[42], [44]	3.137	8.1	–325.8	840	
This work	3.137	8.105	–319.6	–844.2	–7.184

[a]Reference [46] specifies $A_\parallel$ and $A_\perp$ in units of 10^4 cm^{-1}, while MHz seems more appropriate.

Here, χ is the population difference between the initial and final state, which is given by a Boltzmann distribution in thermal equilibrium, as described in Appendix D. By choosing $\boldsymbol{B_1}$ according to different excitation geometries realized in the experiments, the selection rules and transition probabilities can be simulated. Details on the experimental configuration, as well as the analysis of the selection rules and transition probabilities, are given in Sec. IV C.

Previous studies on Er:$LiYF_4$ utilized different experimental techniques to determine the parameters entering the spin Hamiltonian. They include cavity-based EPR spectroscopy [32,39–41], polarized excitation spectra [35], magneto-optical spectroscopy [42,43], optical vector network analysis [44], and Fourier-transform spectroscopy [45]. The published spin Hamiltonian parameters for Er:$LiYF_4$ are summarized in Table I, excluding Refs. [43,45] as these provide the crystal field Hamiltonian parameters. In references specifying the spin Hamiltonian parameters, the quadrupole interaction has been neglected. As shown below, this leads to a significant discrepancy between theory and experiment, particularly in the low magnetic field range. In contrast, studies based on the crystal field calculations usually include the quadrupole interaction [43,45]. However, they do not provide the parameters entering the spin Hamiltonian and hence do not allow for any comparison to the parameters obtained in this work. A particular strength of our study is the fact that all parameters determining the splitting in the absence of a magnetic field can be derived in a single experiment with high precision. Obviously, for determining $g_\perp$ and $g_\parallel$, at least two experiments with different orientations of the crystal are needed.

IV. RESULTS AND DISCUSSION

A. Background subtraction

As described above, we determine the microwave transmission across our setup by measuring the complex scattering parameter S_{21} as a function of frequency at a constant applied magnetic field via a VNA. Besides information on the sample properties, the measured $S_{21}(f)$ dependence is also affected by the characteristic spectral features of the individual microwave components included in the microwave path, caused, e.g., by a finite impedance mismatch. While such contributions can be removed by a thorough microwave

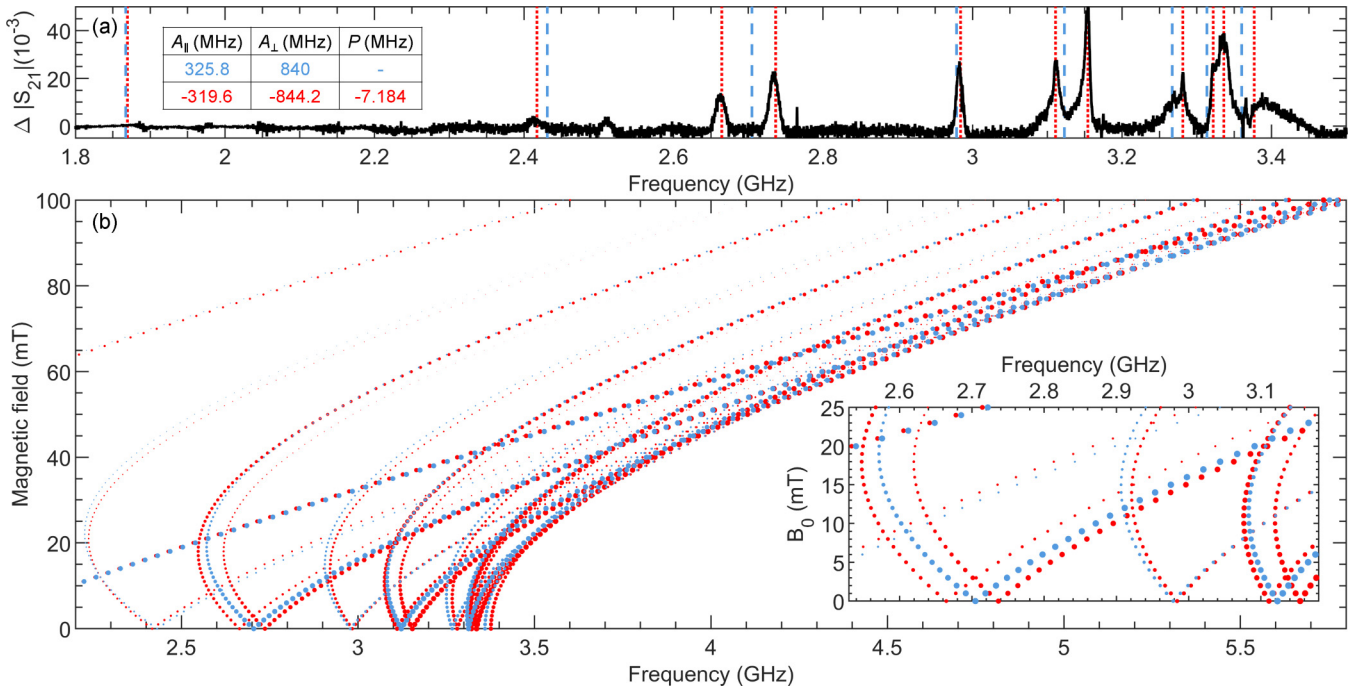


FIG. 2. (a) Background-subtracted zero-field spectrum (black) measured between 1.8 GHz and 3.5 GHz. The blue-dashed and the red-dotted vertical lines mark the simulated transition frequencies utilizing the published spin Hamiltonian parameters [32] and those obtained by fitting our experimental data, respectively. (b) Simulated magnetic field dependence of the hyperfine transition frequencies for $\boldsymbol{B_0} \parallel \boldsymbol{c}$ using the same color code as in (a). The inset shows a zoom-in of the frequency range 2.5–3.2 GHz and magnetic field range 0–25 mT. Note that neglecting the quadrupole interaction parameter P leads to a significant discrepancy between experimental and calculated transition frequencies particularly in the low-field regime.

calibration, this is very challenging in practice due to the complexity of the setup and the wide frequency range of our experiments. To disentangle the signal contributions owing to the spin system from those related to the microwave setup, we follow the simple approach of subtracting a reference background $|S_{21,\mathrm{ref}}(f)|$ from the microwave spectrum $|S_{21,B_i}(f)|$ at each magnetic field. Similar approaches for subtraction-based background removal were used in Refs. [21,47]. As our magnetic field range is limited to $B_0 = 50$ mT, it is not possible to take a reference spectrum at a magnetic field strength where no spin absorption is present within the frequency range of interest. Therefore, we construct the reference spectrum $S_{21,\mathrm{ref}}(f)$ by selecting specific parts of the spectra ($S_{21,B_i}(f)$), which have been measured at different magnetic field strengths where no absorption by the spin system is present. In this way, a reference background $|S_{21,\mathrm{ref}}(f)|$ is constructed, representing the transmission pattern of the overall microwave circuit. Accordingly, we obtain the background-corrected microwave transmission to

$$\Delta\left|S_{21,B_i}(f)\right| = |S_{21,\mathrm{ref}}(f)| - \left|S_{21,B_i}(f)\right|. \tag{3}$$

Note that $\Delta|S_{21}(f)|$ is related only to the effective change in microwave transmission due to the absorption by the spin ensemble, i.e., it contains only the magnetic field-dependent information, which we associate with the spin system. A more detailed discussion on how the background removal technique can affect the extracted parameters is given in Appendix A.

B. Zero magnetic field spectroscopy

In a superconducting coil, a nonvanishing magnetic field can appear because of trapped magnetic flux even in the absence of an applied current. We obtain "zero-field" spectra by measuring the microwave transmission after a thermal quench of the magnet, while at the same time, the earth's magnetic field is attenuated by three layers of magnetic shielding down to approx. 50 nT [28]. Additionally, we perform magnetic field sweeps from negative to positive magnetic field values to identify the effective zero-field value for the powered magnet. The background-subtracted zero-field spectrum measured in the frequency range 1.8–3.5 GHz is plotted in Fig. 2(a) as the black-solid line. To extract the parameters entering the spin Hamiltonian from this data, we numerically calculate the corresponding frequencies of the allowed EPR transitions as described in Sec. III. Since the hyperfine and quadrupole interactions are field independent, they determine the energy level splitting at zero magnetic field, while the Zeeman interaction dominates at higher magnetic field strengths. We extract the refined quadrupole and hyperfine parameters via a non-linear least squares fitting routine of the calculated transition frequencies to the measured zero-field spectrum. We obtain $A_\parallel = -319.6\,\mathrm{MHz} \pm 8.68\,\mathrm{kHz}$, $A_\perp = -844.2\,\mathrm{MHz} \pm 9.44\,\mathrm{kHz}$, and $P = -7.184\,\mathrm{MHz} \pm 1.09\,\mathrm{kHz}$, with the error of the respective parameter indicating the extracted standard deviation from the fitting routine. Furthermore, we find the ratio $g_\parallel A_\perp / g_\perp A_\parallel = 1.023$, indicating that J-state mixing can be neglected [32,48,49]. The negative sign of $A_\parallel$, $A_\perp$, and P is chosen for various reasons. First, it matches the symmetry

rule $\frac{A_\parallel}{g_\parallel} = \frac{A_\perp}{g_\perp} = \frac{A_J}{g_J}$ with $A_J = -125.3\,\mathrm{MHz}$ and the erbium Landé g factor $g_J = 6/5$ [36]. Moreover, the negative sign reproduces the energy level splitting given in Ref. [43]. By studying several ^{167}Er:^{7}LiYF$_4$ crystals from different growth batches also with different doping concentrations (15 ppm and 50 ppm), we can confirm that the hyperfine and quadrupole parameters stated in this work consistently converge for all of the measured crystals.

As changes in dielectric and magnetic properties of crystals directly affect the measured microwave transmission, we have also compared the microwave transmission measured at 8 mK and 4 K, respectively. As discussed in Appendix E, we have found no noticeable change in the measured transmission data. Thus, we exclude a significant change in the dielectric properties and the presence of magnetic phase transitions.

In Fig. 2(a), the blue-dashed lines indicate calculated transition frequencies by taking into account the Hamiltonian parameters from Ref. [32], which do not include the quadrupole interaction ($P = 0\,\mathrm{MHz}$). The red-dotted lines are the transition frequencies calculated by taking into account the Hamiltonian parameters derived in this work, including the quadrupole interaction ($P = -7.184\,\mathrm{MHz}$). Comparison of the measured zero-field spectrum to the calculated transition frequencies indicates a significantly better matching of the transition frequencies extracted with the spin Hamiltonian parameters of the present study. The significant impact of the quadrupole interaction on the zero-field spectrum can be clearly seen and is most prominent for those transitions splitting into two peaks, for example, between 2.6 GHz and 2.8 GHz. In general, the fitted spin Hamiltonian parameters $A_\perp$, $A_\parallel$, and P reproduce the measured transition frequencies well. However, it is also visible that some of the absorption peaks exhibit an additional fine structure. This observation provides evidence that there is an additional interaction, which is not yet included in the Hamiltonian of Eq. (1). Its origin can be manifold, with likely candidates being the superhyperfine interaction with the nuclear spins of the neighboring fluorine ions, as described for Nd:LiYF$_4$ [50], the interaction with other paramagnetic impurities, the change of local symmetries, or higher order terms in the Hamiltonian. The presence of a fine structure, moreover, implies a larger error of the fitted parameters, as compared to the ones specified from the fitting procedure, due to the uncertainty of the extracted peak frequency.

C. Magnetic field dependence

To further highlight the significance of the quadrupole interaction, we analyze the magnetic field dependence of the hyperfine transitions in the magnetic field range 0–100 mT for the two previously compared sets of spin Hamiltonian parameters, i.e., those published in Ref. [32] neglecting the quadrupole interaction and the ones determined in this work, which have been used for the calculated spectra shown in Fig. 2(b). The discrepancies between the simulated frequencies obtained with the parameters published in Ref. [32] (blue) and those obtained in this work (red) are visible up to approx. $B_0 < 50\,\mathrm{mT}$. In this field range, the parameters of Ref. [32] suggest degenerate transitions, for example, at approx. 2.7 GHz and 3.1 GHz. However, these transitions become split when taking into account a finite quadrupole interaction, as indicated in the inset in Fig. 2(b). It is evident that above $B_0 > 50\,\mathrm{mT}$ both sets of parameters yield closely coinciding transition frequencies. This suggests that in publications neglecting the quadrupole interaction in fitting the data, the derived hyperfine parameters $A_\parallel$ and $A_\perp$ to some extent contain the quadrupole interaction. Note that with increasing magnetic field, the splitting arising from the quadrupole interaction is no longer resolvable due to the substantial intensity reduction in the higher frequency branch, which makes the identification of the line splitting difficult.

To obtain the full set of the spin Hamiltonian parameters, we measured broadband EPR spectra in the magnetic field range 0–50 mT both for $\boldsymbol{B_0} \parallel \boldsymbol{c}$ and $\boldsymbol{B_0} \perp \boldsymbol{c}$. The transmission spectra were taken for four different configurations between external magnetic field, microwave propagation vector $\boldsymbol{k}$, and crystallographic $\boldsymbol{c}$ axis at various fixed magnetic field values separated by field steps of 0.5 mT. Spectra taken in Faraday-like geometry ($\boldsymbol{k} \parallel \boldsymbol{B_0}$) are plotted in Fig. 3(a) for $\boldsymbol{B_0} \parallel \boldsymbol{c}$ and in Fig. 3(c) for $\boldsymbol{B_0} \perp \boldsymbol{c}$, while those taken in Voigt-like geometry ($\boldsymbol{k} \perp \boldsymbol{B_0}$) are plotted in Fig. 3(b) for $\boldsymbol{B_0} \parallel \boldsymbol{c}$ and in Fig. 3(d) for $\boldsymbol{B_0} \perp \boldsymbol{c}$. Although the studied crystals are doped with 98% isotopically purified ^{167}Er, we are able to resolve the $I = 0$ erbium (^{166,168,170}Er) EPR-transitions, demonstrating the high sensitivity of the technique. We utilize the $I = 0$ erbium EPR-transition, indicated by the blue crosses in Fig. 3, to confirm the published g factors $g_\parallel = 3.137$ and $g_\perp = 8.105$ and to extract the misalignment angle $\angle(B, c)$ between $\boldsymbol{B_0}$ and the $\boldsymbol{c}$ axis.

For the $\boldsymbol{B_0} \parallel \boldsymbol{c}$ configuration, the misalignment angle $\angle(B, c)$ was determined to be 3.3° for $\boldsymbol{B_0} \parallel \boldsymbol{c}$, $\boldsymbol{k} \parallel \boldsymbol{B_0}$ [Fig. 3(a)], and 1.3° for $\boldsymbol{B_0} \parallel \boldsymbol{c}, \boldsymbol{k} \perp \boldsymbol{B_0}$ [Fig. 3(b)]. This information is included in the respective simulations. To account for the varying experimental conditions between the different data sets, we adjust the minimal threshold intensity of the simulated transitions included in the plots in Figs. 3(a)–3(d) to represent the experimentally observed transitions. As the utilized background removal technique does not take into account the frequency dependence of the transmission, a quantitative analysis of the extracted intensity and the simulation is not feasible, hence, we restrict the study to a qualitative comparison.

The signal intensity of the measured absorption features depends on the transition probability as given in Eq. (2) as well as on several experimental parameters such as the incident microwave power and the sample temperature. As the sample is placed in an ultralow temperature environment with the temperature of the mixing chamber stage $T_{\mathrm{MXC}} < 10\,\mathrm{mK}$, the actual temperature of the spin ensemble can differ owing to the low thermal conductivity of the sample, a considerable thermal boundary resistance, long spin-lattice-relaxation T_1, and local heating induced by the probing power [44,51].

In our experiment, we estimate the minimal attainable temperature of the spin system to $T_{\mathrm{min}} \approx 20\,\mathrm{mK}$. This value is derived from comparing the dependence of EPR absorption amplitudes on the base temperature of the cryostat to the effective temperature model [Eq. (D1)]. Details of the estimation of the spin ensemble temperature and the underlying model

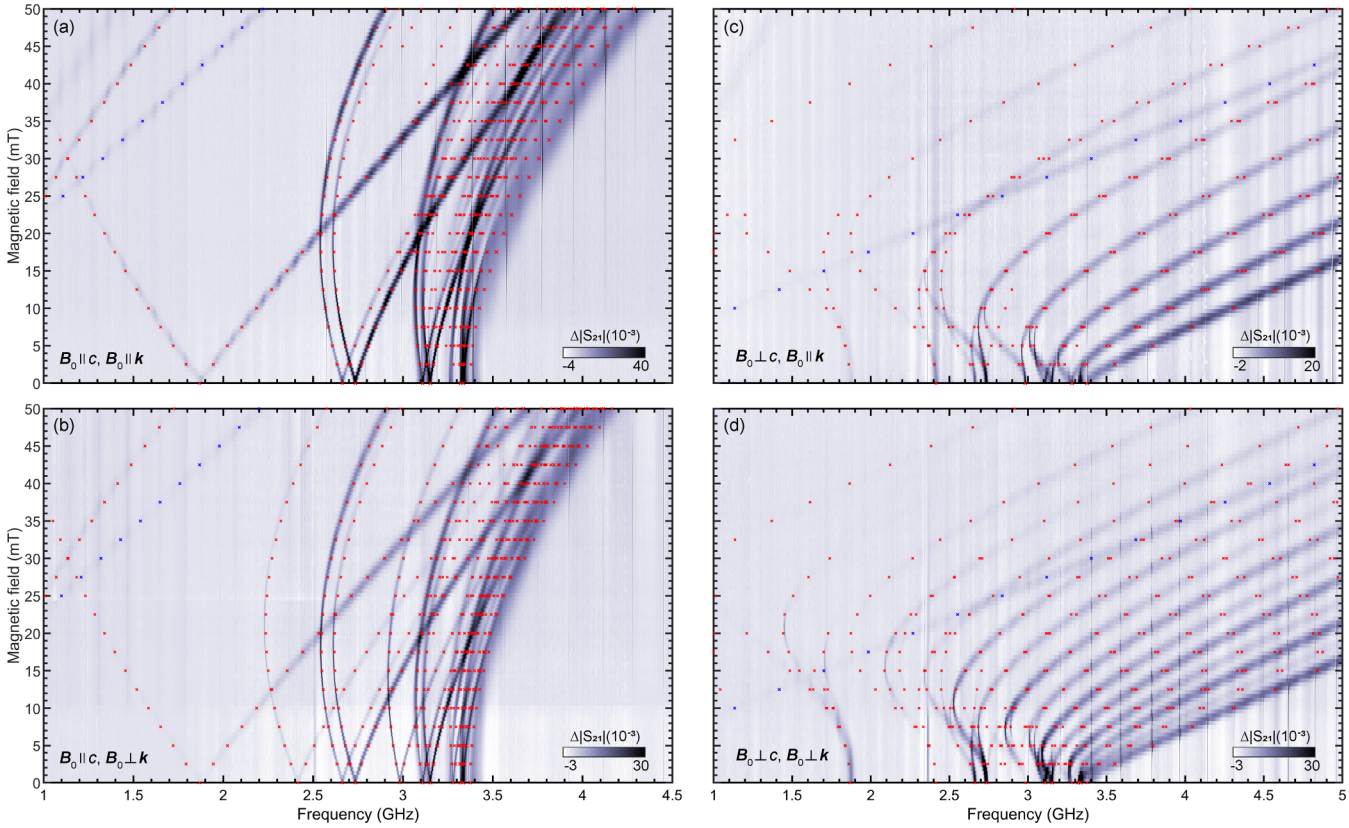


FIG. 3. The broadband EPR spectra measured in the magnetic field range from 0 mT to 50 mT for (a) $\boldsymbol{B_0} \parallel c, \boldsymbol{B_0} \parallel \boldsymbol{k}$; (b) $\boldsymbol{B_0} \parallel c, \boldsymbol{B_0} \perp \boldsymbol{k}$; (c) $\boldsymbol{B_0} \perp c, \boldsymbol{B_0} \parallel k$; (d) $\boldsymbol{B_0} \perp c, \boldsymbol{B_0} \perp \boldsymbol{k}$. The simulated hyperfine ($I = 7/2$) transition frequencies are plotted on top of the measured EPR data with red crosses, while blue crosses represent the erbium-EPR transition for $I = 0$.

are discussed in Appendix D. The simulations of the spin Hamiltonian include $T_{\text{eff}} = T_{\text{min}} = 20\,\text{mK}$.

Comparing the spectra in Fig. 3, a different number of allowed transitions is observed for the different excitation geometries. This is expected, since in Voigt-like geometry [see Figs. 3(b) and 3(d)] excitations in parallel ($\boldsymbol{B_1} \parallel \boldsymbol{B_0}$) as well as in perpendicular ($\boldsymbol{B_1} \perp \boldsymbol{B_0}$) mode are present, while in Faraday-like geometry [see Figs. 3(a) and 3(c)] only perpendicular mode ($\boldsymbol{B_1} \perp \boldsymbol{B_0}$) excitations are probed. A comparative scheme of the experimental alignment for the two configurations is given in Appendix C.

Many experimental EPR spectroscopy studies are performed with perpendicular mode excitation, corresponding in our case to a Faraday-like geometry, with typical EPR frequencies in the X-band (9.5 GHz). Under such experimental conditions, i.e., in the high-field limit, transitions with the selection rules $\Delta m_S = \pm 1$ and $\Delta m_I \neq 0$ are forbidden. They can, however, be allowed in the parallel mode configuration if also a state mixing is present, as is the case for the hyperfine levels of the studied spin system of ^{167}Er:^{7}LiYF$_4$ in the low magnetic field range [52,53]. The different selection rules can be accurately simulated with Eq. (2), when adapting $\boldsymbol{B_1}$ to the respective excitation geometry. Simulating the transition probability with the general magnetic transition dipole moments defined in Ref. [29] for Voigt and Faraday configuration (for unpolarized light) delivers the same result. Furthermore, analytical solutions given in Ref. [36] describe the zero field energy level splitting (for $\boldsymbol{B_0} \parallel \boldsymbol{c}$) well, allowing for a representation of the selection rules in terms of the total angular momentum quantum number $m_F = m_S + m_I$, with $\Delta m_F = \pm 1$ for $\boldsymbol{B_1} \perp \boldsymbol{c}$ and $\Delta m_F = \pm 0$ for $\boldsymbol{B_1} \parallel \boldsymbol{c}$. By analyzing the parallel mode excitations, the sign of P relative to $A_\parallel$ is determined and found to be negative. A more detailed discussion on the selection rules and the hyperfine states involved is out of the scope of this work. We note, however, that the fitted spin Hamiltonian parameters describe the magnetic field dependence of the measured hyperfine transitions with high precision.

D. Linewidth analysis

Besides the frequency of the transition lines, the broadband spectra give direct access to extracting the linewidth of the hyperfine transitions. The linewidth of the spin transitions is limited by various factors, such as the presence of spatially varying strain within the crystal, the distribution of defects, and fluctuations of the local magnetic field. The magnetic noise can, for example, originate from spin flips of surrounding paramagnetic impurities or the nuclear spin bath of the host crystal, in case it contains ions with $I \neq 0$. The inhomogeneous linewidth of optical transitions in isotopically engineered ^{7}LiYF$_4$ was found to be mainly limited by the interaction of the Er^{3+}-ions with local magnetic fields originating from fluorine nuclei in the host lattice [27,35]. Hence, we assume that dipole interactions of this kind dominate the linewidth of the hyperfine transitions also in the microwave

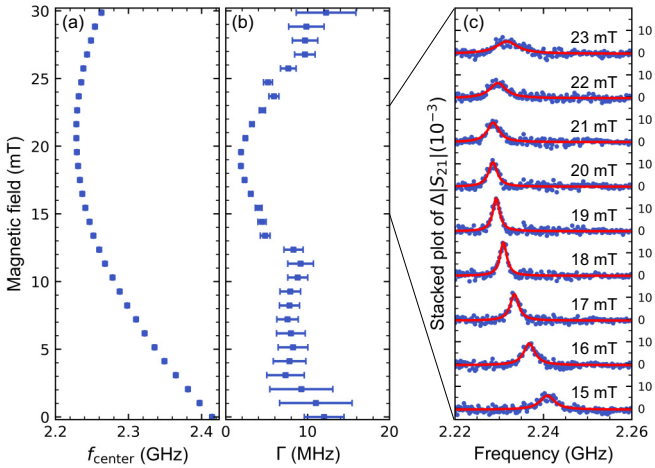


FIG. 4. Experimentally determined magnetic field dependence of the (a) center frequency f_{center} and (b) linewidth Γ extracted from a Lorentzian fit of $\Delta|S_{21}(f)|$. (c) Fitting of the absorption line. Stacked plot of the measured $\Delta|S_{21}(f)|$ (blue data points), while the red line indicates the Lorentzian fit at the indicated magnetic fields. The magnitude of $\Delta|S_{21}|$ for each measured trace is indicated on the right.

range. Other effects contributing to linewidth broadening, such as charge defects, which are the main linewidth broadening mechanism for Er:$CaWO_4$ [54], are assumed to be less relevant for ^{167}Er:^{7}$LiYF_4$. The reason is that the substitution of Y^{3+} by Er^{3+} does not require any charge compensation as both ions are in the trivalent state [33].

We find several transitions that exhibit a narrowing of the linewidth with increasing magnetic field up to the magnetic field value, where the slope of the transition frequency vs magnetic field dependence vanishes, $\partial f_{\text{center}}/\partial B_0 \to 0$. Above this value, the linewidth increases again with increasing field. Because of the plethora of hyperfine transitions exhibiting such behavior, we further exemplary analyze the magnetic field dependence of the linewidth of the $f_{B_0=0\,\text{mT}} = 2.415\,\text{GHz}$ transition for the orientation $\boldsymbol{B_0} \parallel \boldsymbol{c}$ and $\boldsymbol{k} \perp \boldsymbol{c}$. This transition was previously identified to exhibit a ZEFOZ behavior at such a turning point at approximately $B_0 \simeq 20\,\text{mT}$ [44].

The magnetic field dependence of the linewidth Γ [extracted as the full width at half maximum (FWHM) of the Lorentzian lineshape, as indicated in the raw data overlayed by the fit in Fig. 4(c)] of the respective transition in the magnetic field range $B_0 = 0$–$30\,\text{mT}$, is shown in Fig. 4(b). The variation of the transition frequency as a function of the applied magnetic field is plotted in Fig. 4(a). We find that Γ decreases with increasing magnetic field with a minimal linewidth $\Gamma_{B_0\simeq 19\,\text{mT}} = 1.84\,\text{MHz}$. This result reproduces the linewidth dependence reported in [44]. While the mentioned electromagnetically induced transparency study extracted the minimal broadening of the spin transition to be $\Gamma_{\text{HF0}} \simeq 2\pi \times 4.5\,\text{MHz}$, the substantially lower linewidth in the present study can possibly arise due to the lower spin temperature and smaller magnetic noise of the environment. However, as mentioned in Appendix A, the extracted linewidth is prone to significant uncertainty due to the utilized background removal. We attribute the observed linewidth narrowing to a reduced sensitivity to magnetic field fluctuations, which is present at the ZEFOZ point [17]. We further attribute the slight discrepancy between $B_{\Gamma,\text{min}} \simeq 19\,\text{mT}$ and the turning point of the transition frequency $B_{S_1\to 0} \simeq 20.5\,\text{mT}$ to a finite misalignment of the crystallographic axes of the host crystal with respect to the direction of the applied magnetic field, since a true ZEFOZ transition is possible only for perfect spatial alignment in all three spatial dimensions [55]. The importance of a precise alignment of the magnetic field was also pointed out by Fraval *et al.* [56] for a clock transition in Pr^{3+}:Y_2SiO_5. As mentioned above, we have determined a misalignment angle of $\angle(B, c) \simeq 3.3^\circ$, which results in a significant deviation from the conditions for a true ZEFOZ point.

V. OUTLOOK AND CONCLUSIONS

In conclusion, we have performed broadband EPR spectroscopy on ^{167}Er:^{7}$LiYF_4$ single crystals coupled to a superconducting coplanar transmission line at a cryogenic temperature of 10 mK. By sweeping the magnetic field in the range $B_0 = 0$–$50\,\text{mT}$ with different orientations of the magnetic field relative to the microwave propagation vector and the crystal *c*-axis, we are able to obtain very precise, refined parameters for the Zeeman, hyperfine, and quadrupole interaction entering the spin Hamiltonian. Most importantly, we find that it is required to take into account the quadrupole interaction for correctly fitting the measured spectra. This is particularly true for the low magnetic field range.

We further analyze the linewidth of the $f_{B_0=0\,\text{mT}} = 2.415\,\text{GHz}$ hyperfine transition around its ZEFOZ point and find clear evidence for a narrowing of the linewidth down to 1.84 MHz. While the detailed origin of an additional fine-structure visible at zero and low magnetic field still remains open, we demonstrate that broadband EPR spectroscopy at ultralow temperature is a versatile and extremely powerful tool for the investigation and precise characterization of the hyperfine transitions of diluted rare-earth spin ensembles, their selection rules, and linewidth. Because of the strongly increased population difference between the initial and final states, a high signal intensity is obtained, making low-power microwave spectroscopy measurements possible. Moreover, the broadband nature of this technique allows one to directly address various hyperfine transitions simultaneously, potentially at their ZEFOZ point. This makes this technique very promising for microwave quantum memory applications.

ACKNOWLEDGMENTS

We thank Stella Korableva, Oleg Morozov, and Alexey Kalachev for providing the ^{167}Er:^{7}$LiYF_4$ crystals and for valuable scientific discussions. We further thank Owen Huisman for the design of the CPW. We acknowledge support by the Deutsche Forschungsgemeinschaft via Germany's Excellence Strategy (Grant No. EXC-2111- 390814868) and the Bundesministerium für Bildung und Forschung via the project QuaMToMe (Grant No. 16KISQ036).

DATA AVAILABILITY

The data that support the findings of this article are not publicly available upon publication because it is not technically feasible and/or the cost of preparing, depositing, and hosting the data would be prohibitive within the terms of this research project. The data are available from the authors upon reasonable request.

APPENDIX A: BACKGROUND SUBTRACTION

In our broadband experiments, we removed background contributions related to spectral features of the microwave setup by subtracting a reference background from each measured trace, as described by Eq. (3).

We point out that it has been analyzed in Ref. [57] how different background removal methods affect the extracted resonance frequency and linewidth for the case of ferromagnetic resonance experiments conducted with CPWs. The simple subtraction approach (as applied in this work) was shown to have a relative error of around 1% for extracting the resonance frequency and a relative error of up to 10% for the extraction of the linewidth [57]. Therefore, we assume that the transition frequencies extracted in our study are reasonably accurate. However, we also point out that there may be a significant uncertainty in the extracted linewidth.

APPENDIX B: CALIBRATION OF THE MAGNETIC FIELD

To calibrate the strength of the magnetic field, we rely on the EPR transition of a 2,2-diphenyl-1-picrylhydrazyl (DPPH) sample (Sigma Aldrich), which is placed next to the crystal on top of the superconducting CPW. DPPH is a commonly used magnetic field reference material for EPR spectroscopy studies with an isotropic g factor of 2.0037 [58]. To get the magnetic field dependence of the transition frequency, we have first fitted the peak corresponding to the EPR transition of DPPH.

Assuming the known g factor of DPPH, this allows to quantify the magnetic field at the location of the DPPH sample, in close proximity to the ^{167}Er:^{7}LiYF$_4$ sample, as depicted in Fig. 5(c). Using this procedure, we obtain a magnetic field calibration for each of the field configurations discussed in the main text, which is crucial for the extraction of exact absolute values of the parameters entering the spin Hamiltonian. Since the SNR of the DPPH signal is very small, we cannot resolve the published drop of the DPPH g factor as published in earlier studies [58]. In the case of a too-low signal intensity of the DPPH signal, we utilize the EPR signal of the erbium isotopes with $I = 0$ to calibrate the magnetic field strength.

APPENDIX C: SAMPLE ALIGNMENT

The alignment of the applied magnetic field $\boldsymbol{B_0}$, the microwave propagation vector $\boldsymbol{k}$ as well as the oscillating microwave field $\boldsymbol{B_1}$ is schematically shown in Figs. 5(a) and 5(b) for the Faraday-like and Voigt-like geometries, respectively. In Faraday-like geometry, the direction of the oscillating microwave magnetic field $\boldsymbol{B_1}$ is always perpendicular to the applied static magnetic field, while in Voigt-like geometry,

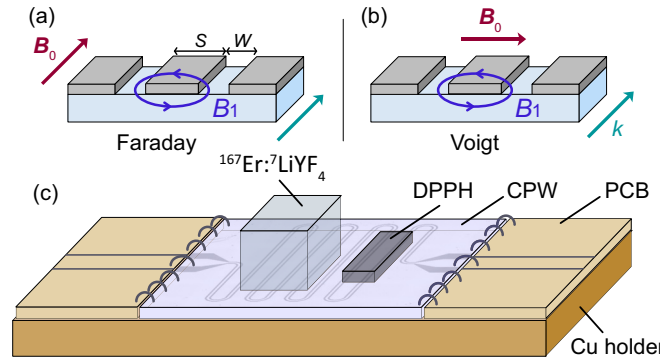


FIG. 5. Relative orientation of the $\boldsymbol{B_0}$, $\mathbf{k}$, and $\boldsymbol{B_1}$ vectors for (a) Faraday-like and (b) Voigt-like geometries. (c) Schematic placement of the ^{167}Er:^{7}LiYF$_4$ crystal and the DPPH sample on top of the CPW.

$\boldsymbol{B_1}$ has both a parallel and perpendicular component. In the CPW design used in our experiments, the width of the central conductor equals $S = 20\,\mu$m, while the width of the gap between the center conductor and the ground is $W = 12\,\mu$m. The placement of the crystal and the DPPH sample on top of the CPW is schematically shown in Fig. 5(c). The CPW is wire-bonded to the printed circuit board (PCB) via the taper patch, while the SMA connectors are then directly connected to the PCBs [not shown in Fig. 5(c) for clarity]. The PCBs and the silicon chip are glued on a copper plate to ensure good thermal coupling to the mixing chamber of the dilution refrigerator.

APPENDIX D: TEMPERATURE DEPENDENCE

A discrepancy between the effective temperature T_{eff} of the spin system and the temperature monitored by the sensor placed on the mixing chamber is a well-known phenomenon. Possible reasons are a low thermal conductivity of the sample, local heating by the applied excitation, and a high thermal boundary resistance between sample and heat sink. To account for this discrepancy, we introduce an effective temperature as introduced in Ref. [44,51],

$$T_{\mathrm{eff}} = T_{\mathrm{min}}(1 + (T/T_{\mathrm{min}})^2)^{1/2}. \tag{D1}$$

Here, T_{min} is the minimal temperature attainable by the spin system, and T indicates the temperature measured by the sensor at the mixing chamber temperature stage. We take broadband spectra at $B_0 = 0\,$mT at different temperatures of the mixing chamber stage and derive the temperature dependence of the peak area of various absorption lines with center frequencies $f = 2.415\,$GHz, $2.663\,$GHz, $2.730\,$GHz, and $2.981\,$GHz, which are plotted in Fig. 6(a). For better comparison, the area of each transition line is normalized to its maximum value. As the change in the peak area relates to the change in the absorption strength, we compare the change in the peak area against the temperature dependence of the spin polarization of the respective transitions. To do so, we follow the steps explained in detail in Ref. [8]. We first calculate the population probability of each of the 16 hyperfine levels in

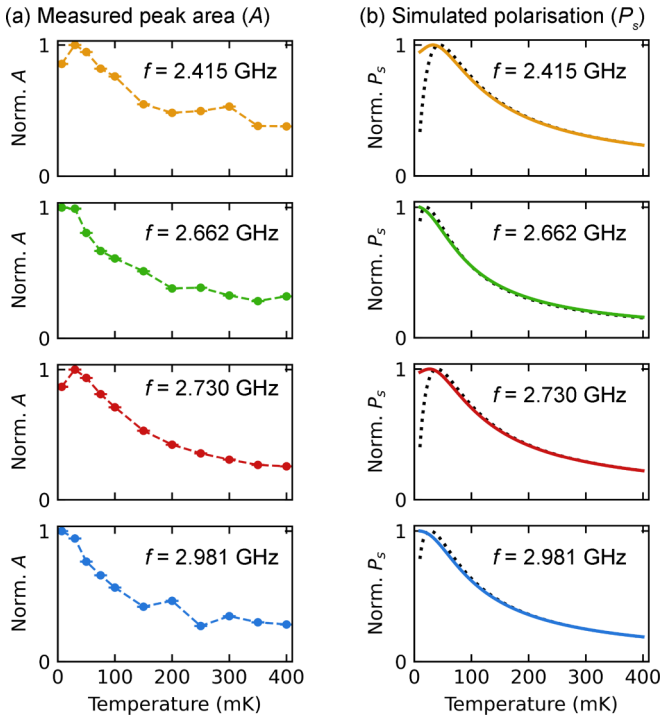


FIG. 6. (a) Temperature dependence of the experimentally determined peak area (A), normalized to its maximum for four absorption peaks with center frequencies $f = 2.415$ GHz, 2.663 GHz, 2.730 GHz and 2.981 GHz at $B_0 = 0$ mT. The dashed line serves as a guide to the eye. (b) Simulated temperature dependence of the spin polarization P_s of the transitions respective to (a), calculated according to Eq. (D3) and normalized to the maximum value. The solid colored line indicates $P_s(T_{\text{eff}})$, while the black dashed line indicates $P_s(T)$.

thermal equilibrium by

$$p_t(T) = \frac{e^{(-E_t/k_B T)}}{\sum_{n=1..16} e^{(-E_n/k_B T)}}, \tag{D2}$$

with the Boltzmann constant k_B and temperature T, and extract the spin polarization $P_s(T)$ of each studied transition as

$$P_s(T) = |p_f(T) - p_i(T)|, \tag{D3}$$

where f and i indicate the final and initial state. To check for the validity of the effective temperature model, we compare the change in peak area to the change in the spin polarization by computing it in two ways: (i) as $P_s(T)$ according to Eq. (D3) by utilizing the temperature of the temperature sensor, indicated as the black dashed line in Fig. 6(b); and (ii) by computing $P_s(T_{\text{eff}})$ according to Eq. (D3) by taking into account T_{eff} from Eq. (D1) with $T_{\text{min}} = 20$ mK, plotted in Fig. 6(b) with the colored solid line. For better comparison, $P_s(T_{\text{eff}})$ and $P_s(T)$ are normalized to their maximum values, respectively.

The close resemblance between the temperature dependence of $P_s(T_{\text{eff}})$ and the experimentally determined peak area and the divergence when accounting for the sensor temperature highlight the necessity of taking the effective temperature into consideration when working at ultralow temperatures. Compared to previous studies on the spin temperature for similar samples in the subkelvin temperature range [27,44,51,59] with observed T_{min} ranging between 70 mK and 500 mK, the extracted $T_{\text{min}} \approx T_{\text{eff}} \approx 20$ mK in this study indicates an efficient cooling of the spin system and a low heating due to the low microwave probing power compared to optical excitation.

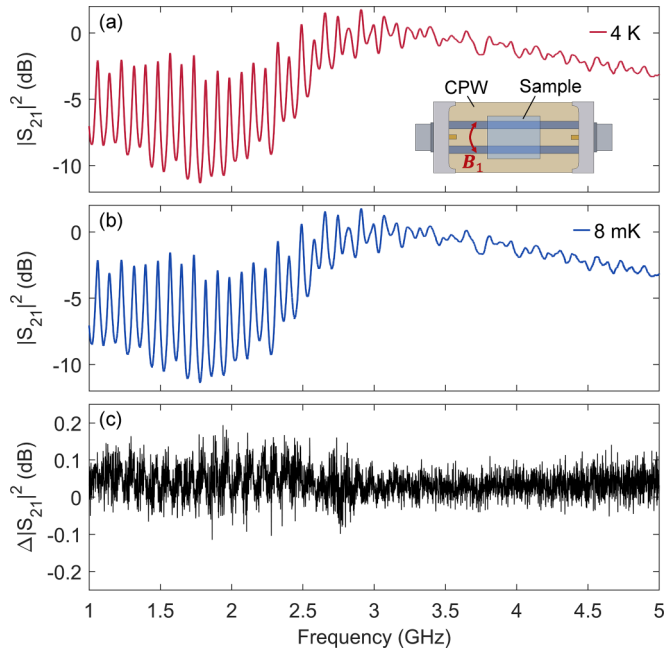


FIG. 7. (a) Measured transmission ($|S_{21}|^2$) of the sample assembly (see inset: schematic of the crystal placed on top of a straight metallic CPW) measured at $T = 4$ K. (b) Measured transmission ($|S_{21}|^2$) of the sample assembly at $T = 8$ mK. (c) Difference in the transmission between (a) and (b) given as $\Delta|S_{21}|^2 = |S_{21}|^2(4\text{K}) - |S_{21}|^2(8\text{ mK})$.

In general, the minimal attainable temperature, and thus the effective temperature of the spin ensemble, can vary between separate cooldowns due to differences in sample mounting and thermal anchoring. For our experiments, we conclude that the extracted effective spin temperature gives a good approximation of the spin temperature at the base temperature and is consistent between different data sets, which follows from the similar intensities of the observed peaks in the spectra taken during different cool-downs.

APPENDIX E: MICROWAVE TRANSMISSION AT SUB-KELVIN TEMPERATURES

In order to assess a potential change in the dielectric properties of the studied crystals at millikelvin temperatures as compared to 4 K, i.e., the temperature regime of most of the previous EPR studies, we compare the microwave transmission measured at 4 K to the transmission measured at 8 mK. For this, a metallic CPW is utilized, as indicated schematically in the inset of Fig. 7(a). Here, we choose the metallic CPW to exclude any changes in the transmission arising from a superconducting layer, e.g., owing to flux trapping.

In such experiments, a change in the relative complex permittivity ϵ_r and permeability μ_r of the sample

can be traced from a change in the measured microwave transmission ($|S_{21}|^2$) of the transmission line. The impedance in the region covered by the sample is given as $Z \propto Z_0\sqrt{\mu_r/\epsilon_r}$ with Z_0 indicating the characteristic impedance in the region not covered by the sample crystal [57,60].

The measured transmission at $B_0 = 0\,\mathrm{mT}$ for $T = 4\,\mathrm{K}$ is indicated in Fig. 7(a), while the $T = 8\,\mathrm{mK}$ transmission is depicted in Fig. 7(b). The difference in the transmission $\Delta|S_{21}|^2 = |S_{21}|^2(T = 4\,\mathrm{K}) - |S_{21}|^2(T = 8\,\mathrm{mK})$ is given in Fig. 7(c).

We observe no change in the microwave transmission that exceeds the noise floor in the data, thus indicating no significant change in the dielectric properties of the sample. Furthermore, the presence of magnetic phase transitions in the evaluated temperature range can be excluded as the spin signatures can be quantitatively understood, as pointed out in Sec. IV C.

[1] G. Kurizki, P. Bertet, Y. Kubo, K. Mølmer, D. Petrosyan, P. Rabl, and J. Schmiedmayer, Quantum technologies with hybrid systems, Proc. Natl. Acad. Sci. USA **112**, 3866 (2015).

[2] E. Gouzien and N. Sangouard, Factoring 2048-bit RSA integers in 177 days with 13436 qubits and a multimode memory, Phys. Rev. Lett. **127**, 140503 (2021).

[3] P. Krantz, M. Kjaergaard, F. Yan, T. P. Orlando, S. Gustavsson, and W. D. Oliver, A quantum engineer's guide to superconducting qubits, Appl. Phys. Rev. **6**, 021318 (2019).

[4] A. Schneider, T. Wolz, M. Pfirrmann, M. Spiecker, H. Rotzinger, A. V. Ustinov, and M. Weides, Transmon qubit in a magnetic field: Evolution of coherence and transition frequency, Phys. Rev. Res. **1**, 023003 (2019).

[5] Y. Kubo, C. Grezes, A. Dewes, T. Umeda, J. Isoya, H. Sumiya, N. Morishita, H. Abe, S. Onoda, T. Ohshima, V. Jacques, A. Dréau, J.-F. Roch, I. Diniz, A. Auffeves, D. Vion, D. Esteve, and P. Bertet, Hybrid quantum circuit with a superconducting qubit coupled to a spin ensemble, Phys. Rev. Lett. **107**, 220501 (2011).

[6] C. Grezes, B. Julsgaard, Y. Kubo, M. Stern, T. Umeda, J. Isoya, H. Sumiya, H. Abe, S. Onoda, T. Ohshima, V. Jacques, J. Esteve, D. Vion, D. Esteve, K. Mølmer, and P. Bertet, Multimode storage and retrieval of microwave fields in a spin ensemble, Phys. Rev. X **4**, 021049 (2014).

[7] J. O'Sullivan, O. W. Kennedy, C. W. Zollitsch, M. Šimėnas, C. N. Thomas, L. V. Abdurakhimov, S. Withington, and J. J. L. Morton, Spin-Resonance linewidths of bismuth donors in silicon coupled to planar microresonators, Phys. Rev. Appl. **14**, 064050 (2020).

[8] C. W. Zollitsch, K. Mueller, D. P. Franke, S. T. B. Goennenwein, M. S. Brandt, R. Gross, and H. Huebl, High cooperativity coupling between a phosphorus donor spin ensemble and a superconducting microwave resonator, Appl. Phys. Lett. **107**, 142105 (2015).

[9] S. Weichselbaumer, M. Zens, C. W. Zollitsch, M. S. Brandt, S. Rotter, R. Gross, and H. Huebl, Echo trains in pulsed electron spin resonance of a strongly coupled spin ensemble, Phys. Rev. Lett. **125**, 137701 (2020).

[10] G. Wolfowicz, H. Maier-Flaig, R. Marino, A. Ferrier, H. Vezin, J. J. L. Morton, and P. Goldner, Coherent storage of microwave excitations in rare-earth nuclear spins, Phys. Rev. Lett. **114**, 170503 (2015).

[11] M. Afzelius, N. Sangouard, G. Johansson, M. U. Staudt, and C. M. Wilson, Proposal for a coherent quantum memory for propagating microwave photons, New J. Phys. **15**, 065008 (2013).

[12] S. Probst, H. Rotzinger, A. V. Ustinov, and P. A. Bushev, Microwave multimode memory with an erbium spin ensemble, Phys. Rev. B **92**, 014421 (2015).

[13] M. Le Dantec, M. Rančić, S. Lin, E. Billaud, V. Ranjan, D. Flanigan, S. Bertaina, T. Chanelière, P. Goldner, A. Erb *et al.*, Twenty-three–millisecond electron spin coherence of erbium ions in a natural-abundance crystal, Sci. Adv. **7**, eabj9786 (2021).

[14] B. Merkel, P. Cova Fariña, and A. Reiserer, Dynamical decoupling of spin ensembles with strong anisotropic interactions, Phys. Rev. Lett. **127**, 030501 (2021).

[15] G. Wolfowicz, A. M. Tyryshkin, R. E. George, H. Riemann, N. V. Abrosimov, P. Becker, H.-J. Pohl, M. L. W. Thewalt, S. A. Lyon, and J. J. L. Morton, Atomic clock transitions in silicon-based spin qubits, Nat. Nanotechnol. **8**, 561 (2013).

[16] A. Ortu, A. Tiranov, S. Welinski, F. Fröwis, N. Gisin, A. Ferrier, P. Goldner, and M. Afzelius, Simultaneous coherence enhancement of optical and microwave transitions in solid-state electronic spins, Nat. Mater. **17**, 671 (2018).

[17] D. L. McAuslan, J. G. Bartholomew, M. J. Sellars, and J. J. Longdell, Reducing decoherence in optical and spin transitions in rare-earth-metal-ion–doped materials, Phys. Rev. A **85**, 032339 (2012).

[18] J. V. Rakonjac, Y.-H. Chen, S. P. Horvath, and J. J. Longdell, Long spin coherence times in the ground state and in an optically excited state of $^{167}Er^{3+}:Y_2SiO_5$ at zero magnetic field, Phys. Rev. B **101**, 184430 (2020).

[19] Y. Alizadeh, J.-P. R. Wells, M. F. Reid, A. Ferrier, and P. Goldner, Zeeman spectroscopy and crystal-field analysis of low symmetry centres in Nd^{3+} doped Y_2SiO_5, J. Phys.: Condens. Matter **35**, 305502 (2023).

[20] C. Clauss, D. Bothner, D. Koelle, R. Kleiner, L. Bogani, M. Scheffler, and M. Dressel, Broadband electron spin resonance from 500 MHz to 40 GHz using superconducting coplanar waveguides, Appl. Phys. Lett. **102**, 162601 (2013).

[21] M. Prinz-Zwick, B. G. Szigeti, T. Gimpel, D. Ehlers, V. Tsurkan, A. O. Leonov, B. Miksch, M. Scheffler, I. Stasinopoulos, D. Grundler, I. Kézsmárki, N. Büttgen, and H.-A. Krug von Nidda, Nuclear and electron spin resonance studies on skyrmion-hosting lacunar spinels, Phys. Status Solidi (b) **259**, 2100170 (2022).

[22] Y. Wiemann, J. Simmendinger, C. Clauss, L. Bogani, D. Bothner, D. Koelle, R. Kleiner, M. Dressel, and M. Scheffler, Observing electron spin resonance between 0.1 and 67 GHz at temperatures between 50 mK and 300 K using broadband

metallic coplanar waveguides, Appl. Phys. Lett. **106**, 193505 (2015).

[23] K. Jing, Z. Lan, Z. Shi, S. Mu, X. Qin, X. Rong, and J. Du, Broadband electron paramagnetic resonance spectrometer from 1 to 15 GHz using metallic coplanar waveguide, Rev. Sci. Instrum. **90**, 125109 (2019).

[24] B. Miksch, M. Dressel, and M. Scheffler, Cryogenic frequency-domain electron spin resonance spectrometer based on coplanar waveguides and field modulation, Rev. Sci. Instrum. **91**, 025106 (2020).

[25] H. Maier-Flaig, S. Klingler, C. Dubs, O. Surzhenko, R. Gross, M. Weiler, H. Huebl, and S. T. B. Goennenwein, Temperature-dependent magnetic damping of yttrium iron garnet spheres, Phys. Rev. B **95**, 214423 (2017).

[26] S. Klingler, H. Maier-Flaig, C. Dubs, O. Surzhenko, R. Gross, H. Huebl, S. T. B. Goennenwein, and M. Weiler, Gilbert damping of magnetostatic modes in a yttrium iron garnet sphere, Appl. Phys. Lett. **110**, 092409 (2017).

[27] N. Kukharchyk, D. Sholokhov, O. Morozov, S. L. Korableva, A. A. Kalachev, and P. A. Bushev, Optical coherence of ^{166}Er:^{7}LiYF$_4$ crystal below 1 K, New J. Phys. **20**, 023044 (2018).

[28] L. M. Vogl, Generating small magnetic fields inside an open-end magnetic shielding with a superconducting solenoid magnet, Master's thesis, Technische Universität München, 2023.

[29] J. Nehrkorn, A. Schnegg, K. Holldack, and S. Stoll, General magnetic transition dipole moments for electron paramagnetic resonance, Phys. Rev. Lett. **114**, 010801 (2015).

[30] K. Momma and F. Izumi, *VESTA3* for three-dimensional visualization of crystal, volumetric and morphology data, J. Appl. Crystallogr. **44**, 1272 (2011).

[31] A. Goryunov, A. Popov, N. Khajdukov, and P. Fedorov, Crystal structure of lithium and yttrium complex fluorides, Mater. Res. Bull. **27**, 213 (1992).

[32] J. P. Sattler and J. Nemarich, Electron-paramagnetic-resonance spectra of Nd^{3+}, Dy^{3+}, Er^{3+}, and Yb^{3+} in lithium yttrium fluoride, Phys. Rev. B **4**, 1 (1971).

[33] E. Chukalina and M. Popova, Hyperfine structure of infrared transitions in LiYF$_4$:Er^{3+}, Phys. Lett. A **262**, 191 (1999).

[34] Vishwamittar and S. P. Puri, Interpretation of the crystal-field parameters in a rare-earth substituted LiYF$_4$ crystal, J. Phys. C **7**, 1337 (1974).

[35] R. M. Macfarlane, A. Cassanho, and R. S. Meltzer, Inhomogeneous broadening by nuclear spin fields: A new limit for optical transitions in solids, Phys. Rev. Lett. **69**, 542 (1992).

[36] A. Abragam and B. Bleaney, *Electron Paramagnetic Resonance of Transition Ions*, Oxford Classic Texts in the Physical Sciences (Oxford University Press, Oxford, 2012).

[37] S. Stoll and D. Goldfarb, EPR interactions—Nuclear quadrupole couplings, in *eMagRes* (John Wiley & Sons, Ltd, Hoboken, NJ, 2017), pp. 495–510.

[38] S. Stoll, Computational modeling and least-squares fitting of EPR spectra, in *Multifrequency Electron Paramagnetic Resonance* (John Wiley & Sons, Hoboken, NJ, 2014), Chap. 3, pp. 69–138.

[39] M. R. Brown, K. G. Roots, and W. A. Shand, Energy levels of Er^{3+} in LiYF$_4$, J. Phys. C **2**, 593 (1969).

[40] K. Guedes, K. Krambrock, and J. Gesland, Identification of trivalent rare earth impurities in YF_3, LuF_3 and LiYF$_4$ by electron paramagnetic resonance, J. Alloys Compd. **344**, 251 (2002).

[41] R. Marino, I. Lorgeré, O. Guillot-Noël, H. Vezin, A. Toncelli, M. Tonelli, J.-L. Le Gouët, and P. Goldner, Energy level structure and optical dephasing under magnetic field in Er^{3+}:LiYF$_4$ at 1.5 μm, J. Lumin. **169**, 478 (2016).

[42] V. N. Lisin, A. M. Shegeda, V. V. Samartsev, and S. L. Korableva, Incoherent photon echo in ^{7}LiYF$_4$:$^{167}Er^{3+}$, Laser Phys. **29**, 124005 (2019).

[43] K. I. Gerasimov, M. M. Minnegaliev, B. Z. Malkin, E. I. Baibekov, and S. A. Moiseev, High-resolution magneto-optical spectroscopy of ^{7}LiYF$_4$:$^{167}Er^{3+}$, $^{166}Er^{3+}$ and analysis of hyperfine structure of ultranarrow optical transitions, Phys. Rev. B **94**, 054429 (2016).

[44] N. Kukharchyk, D. Sholokhov, O. Morozov, S. L. Korableva, A. A. Kalachev, and P. A. Bushev, Electromagnetically induced transparency in a mono-isotopic ^{167}Er:^{7}LiYF$_4$ crystal below 1 Kelvin: microwave photonics approach, Opt. Express **28**, 29166 (2020).

[45] M. N. Popova, E. P. Chukalina, B. Z. Malkin, and S. K. Saikin, Experimental and theoretical study of the crystal-field levels and hyperfine and electron-phonon interactions in LiYF$_4$:Er^{3+}, Phys. Rev. B **61**, 7421 (2000).

[46] S.-Y. Wu, Theoretical investigations on the spin Hamiltonian parameters for Er^{3+} ion in LiYF$_4$, Opt. Mater. (Amsterdam) **27**, 99 (2004).

[47] T. Schwarze, J. Waizner, M. Garst, A. Bauer, I. Stasinopoulos, H. Berger, C. Pfleiderer, and D. Grundler, Universal helimagnon and skyrmion excitations in metallic, semiconducting and insulating chiral magnets, Nat. Mater. **14**, 478 (2015).

[48] R. J. Elliott, K. W. H. Stevens, and M. H. L. Pryce, The theory of magnetic resonance experiments on salts of the rare earths, Proc. R. Soc. Lond. A **218**, 553 (1953).

[49] M. M. Abraham, L. A. Boatner, J. O. Ramey, and M. Rappaz, An EPR study of rare-earth impurities in single crystals of the zircon-structure orthophosphates $ScPO_4$, YPO_4, and $LuPO_4$, J. Chem. Phys. **78**, 3 (1983).

[50] R. M. Macfarlane, R. S. Meltzer, and B. Z. Malkin, Optical measurement of the isotope shifts and hyperfine and superhyperfine interactions of Nd in the solid state, Phys. Rev. B **58**, 5692 (1998).

[51] N. Kukharchyk, D. Sholokhov, A. A. Kalachev, and P. A. Bushev, Enhancement of optical coherence in ^{167}Er:Y_2SiO_5 crystal at sub-kelvin temperatures, arXiv:1910.03096.

[52] G. Mitrikas, Y. Sanakis, and N. Ioannidis, Parallel-mode EPR of atomic hydrogen encapsulated in POSS cages, Appl. Magn. Reson. **51**, 1451 (2020).

[53] C. Rudowicz, P. Cecot, and M. Krasowski, Selection rules in electron magnetic resonance (EMR) spectroscopy and related techniques: Fundamentals and applications to modern case systems, Phys. B: Condens. Matter **608**, 412863 (2021).

[54] W. B. Mims, Electric field shift in paramagnetic resonance for four ions in a calcium tungstate lattice, Phys. Rev. **140**, A531 (1965).

[55] E. Fraval, M. J. Sellars, and J. J. Longdell, Method of extending hyperfine coherence times in Pr^{3+}:Y_2SiO_5, Phys. Rev. Lett. **92**, 077601 (2004).

[56] E. Fraval, M. J. Sellars, and J. J. Longdell, Dynamic decoherence control of a solid-state nuclear-quadrupole qubit, Phys. Rev. Lett. **95**, 030506 (2005).

[57] C. Bilzer, T. Devolder, P. Crozat, C. Chappert, S. Cardoso, and P. P. Freitas, Vector network analyzer ferromagnetic resonance of thin films on coplanar waveguides: Comparison of different evaluation methods, J. Appl. Phys. **101**, 074505 (2007).

[58] Z. Velluire-Pellat, E. Maréchal, N. Moulonguet, G. Saïz, G. C. Ménard, S. Kozlov, F. Couëdo, P. Amari, C. Medous, J. Paris *et al.*, Hybrid quantum systems with high-T_c superconducting resonators, Sci. Rep. **13**, 14366 (2023).

[59] A. Mladenov, N. Pankratova, D. Sholokhov, V. Manucharyan, R. Gross, P. A. Bushev, and N. Kukharchyk, Microwave cavity-free hole burning spectroscopy of Er^{3+}:Y_2SiO_5 at millikelvin temperatures, arXiv:2206.03135.

[60] W. Barry, A broad-band, automated, stripline technique for the simultaneous measurement of complex permittivity and permeability, IEEE Trans. Microwave Theory Tech. **34**, 80 (1986).